Journal of
Materials Chemistry A

Materials for energy and sustainability

Accepted Manuscript

This article can be cited before page numbers have been issued, to do this please use: M. C. Vu, H. S. Srinivasan, P. Mirmira, E. S. Doyle, R. J. Gomes and C. Amanchukwu, *J. Mater. Chem. A*, 2026, DOI: 10.1039/D6TA00159A.

ROYAL SOCIETY OF CHEMISTRY

rsc.li/materials-a

View Article Online
DOI: 10.1039/D6TA00159A

A transition-metal-and-solvent-free dual-graphite battery

Minh Canh Vu, Hrishikesh S. Srinivasan, Priyadarshini Mirmira, Emily S. Doyle, Reginaldo J. Gomes, and Chibueze V. Amanchukwu*

Pritzker School of Molecular Engineering, University of Chicago, Chicago, IL 60637, USA.

*Corresponding author: Chibueze V. Amanchukwu. E-mail: chibueze@uchicago.edu.

View Article Online
DOI: 10.1039/D6TA00159A

Abstract

Conventional grid-scale energy-dense batteries are reliant on transition metal ions, volatile and flammable organic solvents, and are not sustainable or easy to recycle. Here, we present a new battery chemistry where graphite serves as both anode and cathode (dual-graphite battery) with no solvents, transition metal ions, or metals as active species. We show that a mixture of low-melting alkali cations (Li, K, Cs)-based bis(fluorosulfonyl)amide (FSA)-based molten salt can support dual graphite batteries. Using spectroscopic and diffraction techniques, we show conclusively that lithium is the only active species that reversibly (de)intercalates at the graphite anode, while FSA (de)intercalation occurs at the graphite cathode. We find that this molten salt can support graphite/graphite cycling for at least 100 cycles especially when the solid electrolyte interface is carefully pre-formed, demonstrating its promise as a solvent-free, inherently energy-dense next-generation dual-ion battery electrolyte.

Keywords: dual-ion battery, dual-graphite battery, transition metal-free battery, molten salt electrolyte, solvent-free electrolyte.

View Article Online
DOI: 10.1039/D6TA00159A

Introduction

The intermittency of renewable energy sources such as solar and wind requires long-duration grid-scale batteries that are cheap, safe, and energy-dense. Lithium-ion batteries (LIBs) have high energy densities and are currently state-of-the-art[1,2] (**Scheme 1**). However, they pose safety hazards because of the volatile and flammable organic solvents that are used as part of the electrolytes[3,4]. Furthermore, they are expensive and are vulnerable to supply chain risk and geopolitical tension because of the reliance on transition metals such as Ni, Co, and Mn[5]. While some have looked to replace these transition metals with 'earth-abundant' metals such as Fe (used in $LiFePO_4$ cathodes), harms remain: Fe must be intensely mined, leading to adverse environmental risks, impacts on water and air contamination, and significant waste, such as iron mine tailings and chemicals[6]. Finally, LIBs are difficult to recycle because of the numerous components that are present in the cell[7,8]. Therefore, next-generation batteries for grid-scale storage must address these challenges of safety, sustainability, and reliance on transition metals.

There are several alternatives to LIBs for grid-scale storage. Sodium-ion batteries (NIB) promise to replace lithium with the incredibly abundant sodium-ion but are still reliant on transition metals such as V, Ni, Mn, and Fe, and are unsafe due to the prevalence of organic solvents[9,10]. Flow batteries, especially state-of-the-art aqueous vanadium flow batteries, are safer but still rely on transition metals, also suffering from low voltages and low energy densities[11,12]. Organic redox flow batteries can eliminate the need for transition metals but are unsafe (due to flammable and volatile organic solvents), and provide low energy densities, while the degradation of the organic species poses long-term cycling concerns[13,14]. Furthermore, the balance of plant cells required and electrolyte rebalancing lead to added costs[15,16]. Therefore, there still appears to be a trade-off between energy density, need for transition metals, and safety.

In response to these challenges, dual-ion batteries (DIBs) are emerging as a promising energy storage solution, characterized by cost-effectiveness, high voltage, and environmental friendliness[17,18]. One particularly attractive variant of DIBs is the dual-graphite battery (DGB), which utilizes graphite as the anode and cathode (**Scheme 1**). DGBs are specifically of interest as graphite can be mined ('natural graphite') or synthesized from a wide variety of precursors ('synthetic graphite')[19]. Furthermore, the absence of transition

View Article Online
DOI: 10.1039/D6TA00159A

metals in DGBs not only reduces their environmental impact but can simplify the recycling process, aligning with the principles of a circular economy[20]. In this battery chemistry, charge is stored via simultaneous cation intercalation at the anode and anion intercalation at the cathode. In conventional LIBs and NIBs, the cathode hosts the active Li or Na, and the electrolyte serves primarily to transport the cation from the cathode to the anode and vice versa. However, in a DIB, the electrolyte serves as the source and sink for the active cationic and anionic species[21], being pivotal in the battery design. Ion concentration in the DIB electrolyte directly impacts capacity and energy density, with high mass fractions of solvent being undesired due to their inability to participate in reversible charge storage, acting as 'dead weight' in the electrolyte; furthermore, electrolyte stability affects Coulombic efficiency and cycling stability [22].

It is important to underscore that anion intercalation in graphite occurs at high voltages (~5V) [23,24]. Therefore, a high electrochemical window becomes essential for the electrolyte system to accommodate cathode materials like graphite coupled with low-working-potential anode materials. Additionally, an ideal electrolyte system should facilitate reversible electrochemical cation intercalation at the anode and anion intercalation at the cathode with high capacity. Therefore, electrolyte design for DGBs must consider crucial factors, including high ionic conductivity, high oxidative stability, high salt concentrations, and safety[5].

Several electrolyte design strategies have been pursued for DGBs. Conventional carbonate-based electrolytes were first used (inherited from LIBs), but the low salt concentration (~1M) led to low capacities, while the poor oxidative stability of carbonate solvents led to degradation at the cathode, and their volatility and flammability led to significant safety hazards. Tong *et al.* demonstrated the potential of concentrated electrolytes in enhancing the performance of sulfone-based electrolytes[25], achieving notable gains in capacity and reversibility. This heightened compatibility was attributed to the formation of a preferential anion-derived solid electrolyte interphase (SEI) layer[26], significantly bolstering the stability of the anode/electrolyte interface. Increasing the salt concentration to form high-concentration electrolytes (HCEs)[27] can increase discharge capacities and push oxidative stability, but inactive solvents are still present, and safety is still a challenge.

View Article Online
DOI: 10.1039/D6TA00159A

Ionic liquids have been explored as part of the electrolyte since they can support a wide electrochemical stability window and are nonvolatile and nonflammable (improved safety). Despite these merits, IL-based electrolytes encounter notable challenges in the context of DIBs[28]. [52]The IL cation competes with the active ion (e.g., Li, K) for intercalation within graphite, which can cause exfoliation of graphitic anodes due to the large size of the bulky IL cation [29]. Furthermore, poor passivation of the Al foil current collector in IL electrolytes based on bis(trifluoromethanesulfonyl)amide ($TFSA^-$) and bis(fluorosulfonyl)amide FSA^- salts leads to corrosion[30–32]. Therefore, enhancing the cycling durability of DGBs requires novel electrolyte designs.

Inorganic molten salts are a promising alternative to address the challenges associated with electrolytes for DGBs[33–36]. These molten salts consist entirely of inorganic cations and are distinct from conventional 'organic ionic liquids' that are reliant on bulky organic cations. They are also solvent-free and intrinsically non-flammable/non-volatile. Additionally, in molten salt electrolytes, all cations (if carefully selected) can be electrochemically active, maximizing the energy density of the electrolyte. Low-melting solvent-free inorganic molten salt electrolytes provide a promising strategy for novel electrolyte development for energy storage, especially batteries operating at intermediate temperatures[37–40]. Amide-based molten salt electrolytes are especially interesting because they have low melting transitions (~45°C) that enable operation at temperatures <100°C.[40,41] In contrast, nitrate-based molten salt electrolytes require operating temperatures of ~150°C[38]. Amide-based molten salt electrolytes [42,43]have been explored for different battery chemistries such as lithium metal batteries and electrodeposition-based DIBs [42], but never for DGBs.

In this work, we propose a new DGB chemistry that is solvent-and-transition metal-free (**Scheme 1**). To enable this, we studied a solventless ternary low-melting-point molten salt electrolyte consisting of LiFSA, KFSA, and CsFSA for DGBs. We discovered that this molten salt electrolyte enables reversible (de)intercalation of Li^+ cation and FSA^- anion within graphite electrodes using a suite of diffraction and spectroscopic techniques. We prove that only Li is the active species, even though K and Cs are also known to independently intercalate into graphite. Furthermore, we show the importance of graphite pre-lithiation and pre-cycling to ensure stable cycling at 80°C at an upper cutoff potential as high as 5.2 V. Our work

View Article Online
DOI: 10.1039/D6TA00159A

pushes the paradigm of battery design for the development and study of novel battery chemistries that consist of earth-abundant materials, that have no transition metals, have no solvents (intrinsically non-flammable/non-volatile), are sustainable, and are easy to recycle.

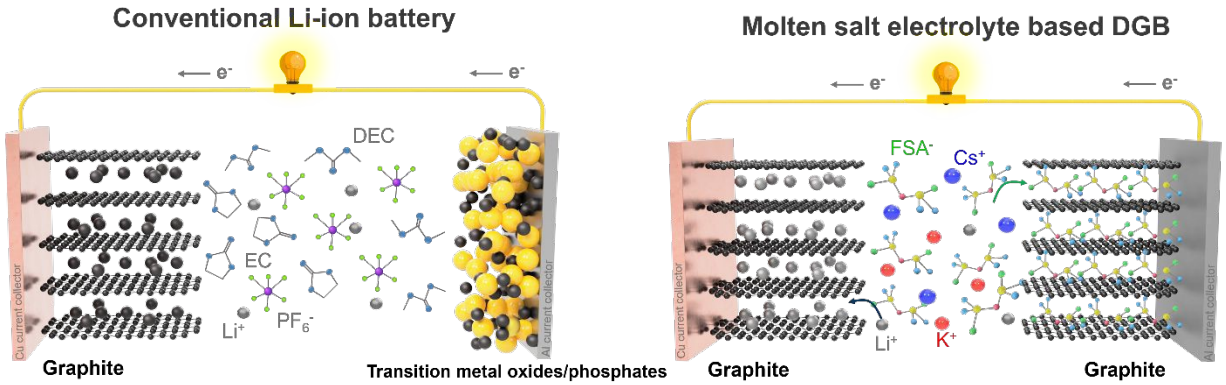

Scheme 1. Illustration of comparison between a conventional liquid electrolyte-based Li-ion battery and a molten salt electrolyte-based dual graphite battery (DGB). PF_6^-: hexafluorophosphate, DEC: diethyl carbonate, EC: ethylene carbonate.

View Article Online
DOI: 10.1039/D6TA00159A

Results and Discussion

Cation intercalation and reversibility in graphite

The influence of molten salt composition on reversible lithium intercalation into graphite was studied using electrochemistry, diffraction, and spectroscopy. Prior work has shown that an alkali cation-based per(fluorosulfonyl)amide-based molten salt electrolyte can support Li-ion batteries[33,43]. However, there was no direct confirmation of ion intercalation. Hence, it remained unclear what the active cation is especially since Li[44], K[45], and Cs[46] can intercalate independently within graphite. Here, we first probe cation intercalation into graphite using Li||GrCu half-cells (graphite coated on Cu current collector) with $Li_{0.30}K_{0.35}Cs_{0.35}FSA$ as the molten salt electrolyte (MSE), which has first been reported by Kubota et al and studied by our group for lithium metal batteries.[40,41] This is the eutectic composition, with a melting point of 45°C, and exhibits an ionic conductivity of 5.64 mS cm^{-1} at 80°C[47].[41] A control electrolyte – $Li_{0.30}K_{0.35}Cs_{0.35}FSA$ dissolved in fluoroethylene carbonate/fluoroethyl methyl carbonate (FEC/FEMC) (3:7 v/v) solvent mixture at a total salt concentration of 3 M (LE)[48] – was used to draw a contrast between alkali cation intercalation in a typical small molecule electrolyte system and the molten salt electrolyte. We chose this solvent mixture as a control, as it has been studied previously at the high voltages needed for anion intercalation.[48] **Figure 1a** and **Figure S1a** in Supporting Information (SI) show charge-discharge voltage curves for alkali cation intercalation from the MSE and the LE, respectively, at a specific current of 20 mA g^{-1}. Note that the operating temperatures for the two electrolytes are different: alkali cation intercalation from the ternary molten salt electrolyte was studied at 80°C compared to 20°C for the LE. All voltages are reported vs. Li/Li^+ unless otherwise stated. Both the LE and MSE provide nearly identical discharge capacities of ~360 mAh g^{-1} during the first cycle, with the LE supporting a higher initial Coulombic efficiency than the ternary MSE (90% vs. 69%, respectively). However, by the second cycle, the Coulombic efficiency of the MSE is higher than that of the LE (99.6% compared to 97.8%), indicating an excellent ability to passivate the graphite electrode and enable reversible alkali cation (de)intercalation[43]. **Figure 1b** and **Figure S1b** in SI illustrate the differential capacity profiles of the first and second cycles of the Li||GrCu half-cells utilizing the MSE and LE, respectively. The stage index denoted as 'n,' represents the compounds formed at different

View Article Online
DOI: 10.1039/D6TA00159A

stages and indicates the number of graphene layers between adjacent intercalant layers. The calculation of the stage index, 'n,' employed equations from previous studies,[49,50] offering valuable insights into the structural evolution and layering during the intercalation/deintercalation processes. There are four distinct peaks during the first cycle charging step for the half-cells with each of the electrolytes, labeled as A, B, C, and D in red. They likely correspond to different graphite stage transitions during intercalation: Stages > 4 (A), Stage 3 (B), Stage 2 (C), and Stage 1 (D)[51] The first cycle stage transitions of the small molecules-based system are shifted to lower potentials compared to those of the molten salt system. The origin of this higher first-cycle overpotential for the small-molecule-based electrolyte compared to the ternary molten salt electrolyte is currently unclear. Stage transitions during the second charging step – labeled as A, B, C, and D in blue – occur at the same potentials as stage transitions during the first charging step for the molten salt electrolyte. However, during the second charging step for the small molecule-based system, each stage transition is shifted to higher potentials than those occurring during the first charging step. Furthermore, there appear to be fewer distinct phase transitions, with peak C appearing to be a convolution of two peaks. Despite this behavior peaks A, C, and D in the second cycle of the ternary molten salt electrolyte largely coincide with peaks A, B, and C in that of the LE, suggesting similar intercalation behavior of a similar set of alkali cation species. Also, the de-intercalation peaks A', B', C', and D' occur at the same potential during both the first and second cycles for both MSE and the LE, which could again suggest the de-intercalation of a similar set of alkali cation species, inducing phase changes in graphite that occur at the same electrochemical conditions.

View Article Online
DOI: 10.1039/D6TA00159A

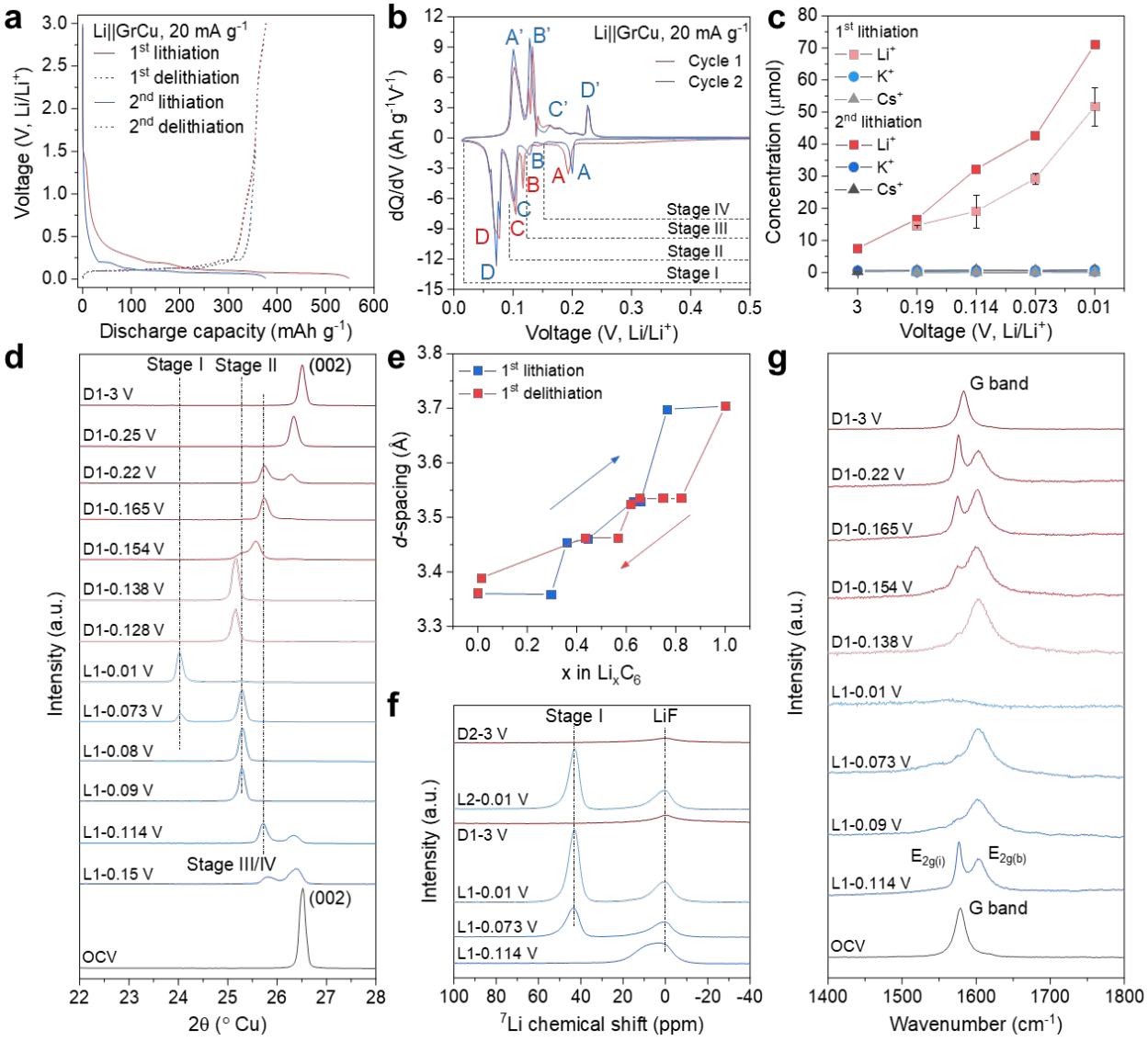

Figure 1. **Cation intercalation**. (a) Charge-discharge voltage profiles, (b) dQ/dV of Li||GrCu cells using MSE at 20 mA g^{-1}. (c) Cation concentrations in the intercalated GrCu electrodes at different stages of charge obtained using ICP-MS from the Li||GrCu cells with MSE at 20 mA g^{-1}. (d) Ex-situ XRD pattern, (e) Interlayer distance, (f) ^{7}Li Solid-state NMR, (g) Raman spectra of the intercalated GrCu electrodes at different stages of charge from the Li||GrCu cells using MSE at 20 mA g^{-1}, respectively.

The question of which alkali cation is intercalating from this multi-cation ternary molten salt system was examined using inductively coupled plasma mass spectrometry (ICP-MS) over different states-of-charge (SOC). The quantity of each alkali cation intercalated into graphite from the ternary molten salt over a range

View Article Online
DOI: 10.1039/D6TA00159A

of half-cell potentials from the open circuit voltage (OCV) to 0.01 V vs. Li/Li$^+$ is reported in **Figure 1c**. Intriguingly, despite the presence of three alkali metal cations in the electrolyte, only Li$^+$ appears to intercalate into graphite. The concentration of Li$^+$ increased with the state-of-charge for both charging cycles, while negligible quantities of K$^+$ and Cs$^+$ were observed even though previous studies have shown that Li$^+$ and K$^+$ can independently (de)intercalate reversibly into graphite in single-cation electrolytes.[45,52,53] Nevertheless, electrochemical Li$^+$ intercalation is thermodynamically preferred over K$^+$ intercalation[54,55], therefore it is unsurprising that Li$^+$ intercalation is preferred during galvanostatic charging over the intercalation of K$^+$ and Cs$^+$. Li$^+$ intercalation into graphite from mixed molten alkali metals is also preferred over the intercalation of other alkali ions[56]; this being a chemical method of intercalation, factors such as solvation energies of the various alkali cations are unlikely to contribute to the facility for Li$^+$ insertion compared to the other alkali cations in electrochemical systems. Ionic radius is also an unlikely contributor to intercalation activity of Li$^+$: Na$^+$, despite being smaller than K$^+$, exhibits poor intercalation capacity without a co-intercalating solvent. Rather, the binding energy between the alkali cation and the graphite has been found to be a descriptor for intercalation activity, with Na$^+$ binding to graphite being energetically unfavorable, and with K$^+$ having a weaker binding energy to graphite compared to Li$^+$.[57,58] Finally, there is enough Li$^+$ in the ternary molten salt electrolyte to charge the graphite to near its theoretical capacity, preventing the intercalation of further ions.

Recently, Mendoza-Cortes *et al.*[54] have used cyclic voltammetry to show that it is possible for Li$^+$ and K$^+$ to co-intercalate into few-layer graphene, especially at a Li$^+$:K$^+$ ratio greater than 1/33 in a propylene carbonate-ethylene carbonate-based electrolyte mixture. Given that the ratio of Li$^+$:K$^+$ in the ternary molten salt electrolyte is much greater than 1/33 (~0.86), it would seem that Li$^+$ and K$^+$ co-intercalation *should* then occur. There are, however, notable differences between the work by Mendoza-Cortes *et al.* and this work. Besides the differences in electrode, Mendoza-Cortes *et al.* investigate alkali cation intercalation using cyclic voltammetry, where the switching potential becomes increasingly negative with decreasing Li$^+$ concentration, whereas this work investigates alkali cation intercalation using galvanostatic cycling with a fixed Li$^+$ concentration and a fixed lower cutoff potential of 0.01 V vs. Li/Li$^+$. This preference of Li$^+$ over

View Article Online
DOI: 10.1039/D6TA00159A

other alkali cations under these conditions is thus likely not unique to this ternary molten salt electrolyte; in fact, as illustrated in **Figure S1c** in SI, Li^+ is the sole alkali cation species present in the graphite electrode upon intercalation from the FEC/FEMC-based liquid electrolyte, which supports this hypothesis.

***Ex situ* structural investigations of alkali cation-graphite intercalation**

The structures of alkali cation graphite intercalation compounds (GICs) were studied using a suite of *ex situ* X-ray diffraction (XRD) and spectroscopic techniques over different SOCs. Intercalated graphite was characterized after charging at a current of 20 mA g^{-1} and subsequently briefly washed with dimethoxyethane (DME) to remove residual salt. The extracted and washed graphite electrodes are shown in **Figure S2** in the SI. Note that in both Figure S2 and **Figure 1d-f**, the prefixes L and D correspond to lithiation and delithiation, while the succeeding digit indicates the cycle index. As shown in **Figure S2** in SI, upon charging to 0.01 V, the color of the graphite electrode changes from black (0.15 V and 0.114 V) to brown (0.09 V and 0.08 V) to a distinct golden color (0.073 V and 0.01 V), which indicates the formation of a LiC_6 GIC[59]. During delithiation, these color changes reverse in order.

Diffractograms of intercalated graphite and the interlayer distance of the graphite planes are shown in **Figure 1d-e**, respectively. At open circuit potential (OCV) before intercalation, only the (002) peak of graphite is present within the depicted 2θ range, occurring at ~26.5°, which corresponds to a d-spacing of 3.36 Å. During ion intercalation, lattice expansion and disruption of the original ordering of graphene planes cause the (002) peak to disappear and new peaks to arise according to the periodic structure of the intercalated ions. Upon charging graphite to 0.15 V, the (002) peak disappears as expected, and two new peaks arise at 25.8° and 26.4° which are assigned to the LiC_{18} and LiC_{24}, respectively. These peaks are unlikely to correspond to KC_8 (2θ at 16.4° and 33.4°)[46,60] and CsC_8 (2θ at 15° and 30°)[46,61]. This once again confirms that Li^+ is the only cation that intercalates from this ternary molten salt electrolyte. Upon further charging to 0.08 V, only one peak at a lower 2θ of 25.3° is present corresponding to LiC_{12}. Finally, at a potential of 0.01 V, the LiC_{12} peak is no longer present, and a new peak arises at 24°, corresponding to a d-spacing of 3.70 Å, which is indicative of LiC_6 formation. During delithiation, graphite experiences stage

View Article Online
DOI: 10.1039/D6TA00159A

transitions in reverse order of what was described for charging, and finally upon full discharge of the graphite, the (002) peak of graphite reappears, suggesting excellent lithium (de)intercalation reversibility. The second charge/discharge process is similar to the first cycle (**Figure S3a** in SI). Cation intercalation from the liquid electrolyte appears largely identical to intercalation from the ternary molten salt electrolyte (**Figure S1d**), with the formation of LiC_6 achieved at a potential of 0.01 V and the (002) peak of graphite reappearing upon full delithiation of the graphite electrode. Again, peaks for K- and Cs-based GICs were not present in these diffractograms either, which once again supports the finding that only Li^+ intercalates into graphite from the multi-cation FEC/FEMC-based electrolyte.

^{7}Li ssNMR spectra of intercalated graphite with the ternary molten salt electrolyte are shown in **Figure 1f**. When the graphite electrode is partially lithiated (charged to 0.114V), a ^{7}Li isotropic chemical shift of 8.5 ppm can be attributed to the Li_xC_6 (LiC_{31}).[54] Upon full lithiation of the graphite electrode, two peaks appear in the ^{7}Li NMR spectrum: one peak at ~43 ppm, which corresponds to the LiC_6 compound, and another, smaller peak at ~2 ppm, which likely originates from ionic compounds comprising the SEI and the remaining salts.[59] The peak intensity at ~43 ppm increases as the graphite structure transfers from LiC_{12} to LiC_6. After fully delithiating the graphite cathode, the LiC_6 peak disappears entirely while the faint peak at ~2 ppm remains. A similar observation can be found for the LE (**Figure S1e** in SI), where a peak at 43 ppm can be assigned to the LiC_6 compound.

Raman spectra of the lithiated graphite electrodes are provided in **Figure 1g**. During intercalation, the graphitic carbon "G band", which occurs at ~1579 cm^{-1}, diminishes in intensity and an additional peak shifted to ~1600 cm^{-1} appears as graphite becomes partially lithiated.[50] These peaks are denoted as $E_{2g(i)}$ and $E_{2g(b)}$, respectively, and represent the vibrational modes of graphitic carbon adjacent to an empty interlayer and graphitic carbon adjacent to an intercalant layer, respectively. In essence, these two distinct peaks arise due to the distinct carbon environments present in partially lithiated graphite. This behavior is evident as the graphite electrode is charged from OCV to 0.073 V with the ternary molten salt electrolyte. Subsequently, the "G band" disappears at a potential of 0.01 V, which has been reported to correspond to LiC_6 formation. After full delithiation to 3V, the G band returns but is slightly blue shifted (higher wavenumbers) due to SEI

View Article Online
DOI: 10.1039/D6TA00159A

formation[62,63]. In comparison, the Raman spectra of the lithiated graphite using LE (**Figure S1f** in SI) also observed the disappearance and re-emergence of the G band after a full charge/discharge cycle.

Reversibility and characteristics of FSA^- anion intercalation

The reversibility and nature of FSA^- anion (de)-intercalation into graphite from the molten salt electrolyte was investigated using cyclic voltammetry (CV) with Li||GrAl cells (graphite coated on aluminum) over a potential window of 3-5.1V vs. Li/Li^+ at 80°C. The first two scans are shown in **Figure 2a**, showcasing redox features that indicate reversibility. During the first cycle, oxidative currents were recorded at an onset potential (defined as the potential where the specific current reached 10 mA g^{-1})[64] of 4.41 V vs. Li/Li^+, subsequently shifting in the following cycle to slightly lower potentials (4.33 V). This observed shift is likely attributed to the "activation" of the graphitic structure, a phenomenon previously studied in the context of anion intercalation from both ionic liquid electrolytes[65–67] and small-molecule-based high-concentration electrolytes (HCE)[68,69]. At higher potentials within the range of 4.65 to 4.95 V, three discernible peaks are observed, indicative of the well-known "stage formation" behavior characterizing acceptor-type GICs.

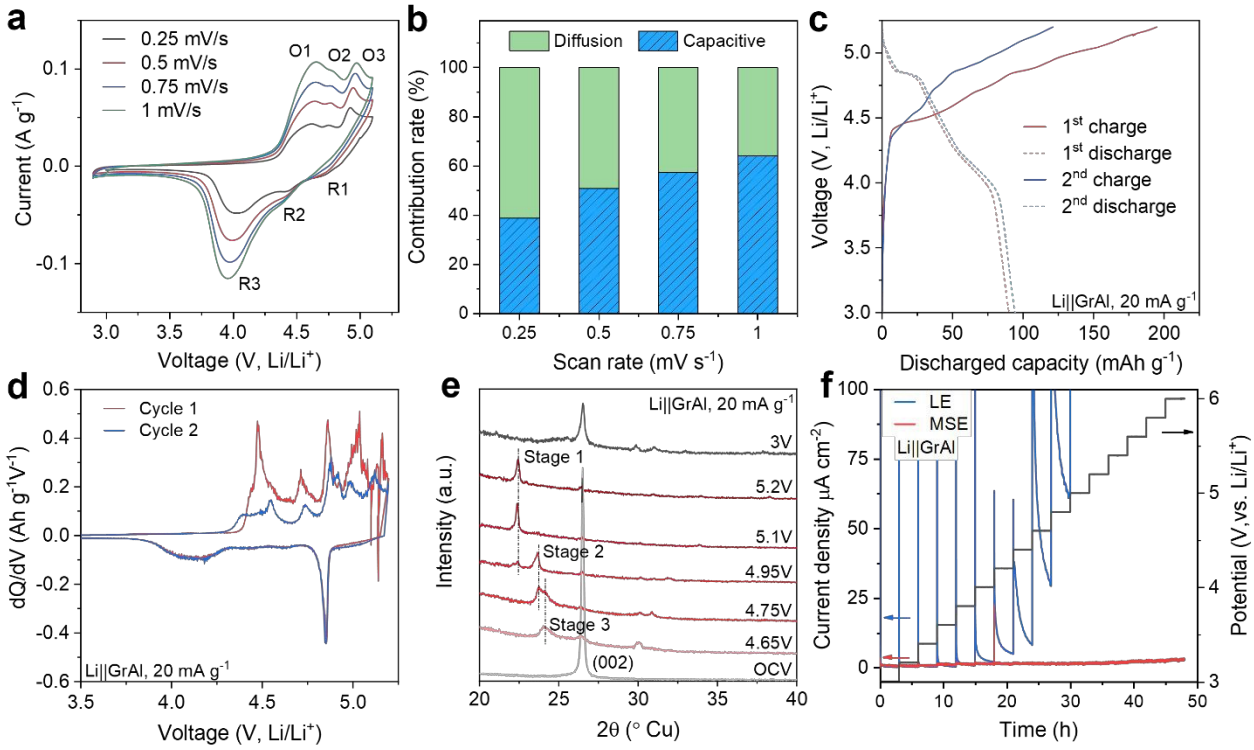

View Article Online
DOI: 10.1039/D6TA00159A

Figure 2. Anion intercalation. (a) Cyclic voltammogram profiles of Li||GrAl cells using MSE at different scan rates. (b) The capacitive and diffusion contribution towards FSA^- storage at different scan rates. (c) Charge-discharge voltage profiles and (d) dQ/dV curves of Li||GrAl cells using MSE at 20 mA g^{-1}. (e) Ex situ XRD pattern of the GrAl electrodes after being charged to 5.2V using MSE at 20 mA g^{-1}. (f) Potenstiostatic hold measurements of the Li||GrAl cells using MSE and LE.

Upon comparing the onset potentials for FSA-GIC formation from ionic liquids (IL; 4.4 V vs. Li/Li^+)[70] and HCE (4.6 V vs. Li/Li^+)[71], it was noted that the onset potential in the molten salt electrolyte was marginally lower (4.33 V vs. Li/Li^+). This disparity may be attributed to the strong solvent–salt interactions prevalent in HCEs. In the cathodic scan, reductive currents were observed within the potential range of 3.9–4.5 V vs. Li/Li^+, indicating reversible de-intercalation of FSA^- anions. To delve into the kinetics of the electrode reaction, different scan rates were applied (**Figure S3b** in SI and **Figure 2a** as the raw data). The results revealed an augmentation in the maximum peak current for both anodic and cathodic specific currents with increasing scan rate. Based on the power-law expression[72], the relationship between the redox peak currents (i) and the scan rates (v) can be presented as:

$$i_p = a v^b \qquad (1)$$

where parameter "b" is an exponent that describes the extent of Faradaic (b = 0.5) and capacitive contributions (b = 1.0) towards the measured current[73]. By constructing a plot of $\log(i_p)$ against $\log(v)$ (**Figure S3b** in SI), the values of "b" for the oxidative (O) and reductive (R) peaks in the Li||GrAl half-cells were determined. These exponents were determined to be in the range of 0.5 – 0.7, which suggests both Faradaic and capacitive contributions towards the overall current, with the capacitive contribution potentially enabling fast intercalation kinetics. Correspondingly, the measured current can be divided into surface-controlled ($k_1 v$) and diffusion-controlled ($k_2 v^{1/2}$) parts by the equation:

$$i_p = k_1 v + k_2 v^{1/2} \qquad (2)$$

View Article Online
DOI: 10.1039/D6TA00159A

By integrating the CV profiles, we can find that the percentage of surface capacitive contribution to the capacity increases with a higher scan rate (**Figure 2b**); e.g. capacitive contribution increases from 38.8% (0.25 mV s^{-1}) to 64.2% (1 mV s^{-1}). The increase in capacitive contribution with rising scan rate is attributed to the kinetics of anion intercalation into graphite. At low scan rates, diffusion-controlled processes dominate and result in extended plateau regions in the GCD profiles. In contrast, as the scan rate increases, diffusion becomes increasingly limited, leading to a reduced contribution from intercalation plateaus and a relative enhancement of surface-controlled (capacitive) processes. This trend is consistent with the shortened or sloping charge–discharge plateaus observed in **Figure S4g** at higher current densities, which indicate incomplete anion intercalation but enhanced capacitive storage near the electrode surface.

The galvanostatic charge-discharge profiles of the Li||GrAl half-cells at 20 mA g^{-1} and 80°C using the molten salt electrolyte are shown in **Figure 2c**. FSA^- intercalation and deintercalation into/from the graphite electrode are denoted as charge and discharge, respectively. In the charging curve, three distinctive potential regions emerge. Initially, a prolonged plateau within the voltage range of 4.4–4.65 V (region I), a series of small plateaus in the voltage range of 4.65–4.95 V (region II), and a pronounced, prolonged plateau in the voltage range of 4.95–5.2 V (region III). The initial plateau region I, below 4.65 V, is attributed to cathode electrolyte interphase (CEI) formation. FSA^- intercalation commences at 4.65 V during the first charging cycle, resulting in a charged capacity of 58 mAh g^{-1}, and continues up to 4.95 V (with a charged capacity of 114 mAh g^{-1}) in the first charging curve. The remaining charging capacity arises from region III, reaching 195 mAh g^{-1} at a cut-off voltage of 5.2 V. Meanwhile, the Li||GrAl cell using LE exhibits a charging capacity of 140 mAh g^{-1} (**Figure S3c** in SI). The corresponding discharging curve (FSA^- deintercalation), comprises four distinct regions: a sloping region from 5.20 to 4.86 V, a prolonged plateau region from 4.86 to 4.81 V, and two sloping regions from 4.81 to 4.25 V and 4.25 to 3.93 V. The onset potential for FSA^- anion deintercalation is observed at 5.1 V, continuing until 3.93 V, with the majority of the discharge capacity obtained in the wide potential range of 5.1–4.25 V. Notably, the charge and discharge curves exhibit differences, where a discharge capacity of 94 mAh g^{-1} is achieved, resulting in an initial CE of ~48% with the MSE compared to ~29% for the LE (**Figure S3c**). Upon comparison with the charge-discharge curves

View Article Online
DOI: 10.1039/D6TA00159A

of the second cycle, a distinctive variation is evident in the voltage range of 4.3–5.2 V during the second charging process. The irreversible capacity noted in the first cycle diminishes after the second cycle. This behavior aligns with previously reported observations for graphite cathodes in both ionic liquid electrolytes and organic HCE.[74,75] Such phenomena are attributed to CEI formation on the electrode surface during the initial charging.

The onset potential for anion intercalation undergoes a notable decrease in the second cycle (4.33 V compared to the 4.41 V observed in the first charging step). This phenomenon is posited to stem from overcoming the significant Van der Waals forces that bind the graphene layers into which the FSA^- anions must intercalate[76]. The accommodation of these comparatively large anions between two adjacent graphene layers demands an elevated activation energy, necessary to overcome the van der Waals forces governing the interaction[76]. However, a shift is observed in subsequent cycles, where the onset for FSA^- intercalation decreases due to mild graphite exfoliation in the first cycle. The overlapping charge–discharge curves indicate a reversible and reproducible pattern in the intercalation of FSA^- between the graphene layers.

Figure 2d shows that differential capacity curves exhibit distinct features, notably the initial peak for anion intercalation observed at 4.48 V, which shifts to 4.55 V in subsequent cycles. Throughout the charging process, multiple current peaks emerge around 4.71, 4.86, 5.03, and 5.15 V. These peaks undergo slight shifts during the second cycle, indicating dynamic changes in the intercalation process. The initial charging curve displays a unique shape compared to the subsequent cycles, attributed to the initial kinetic hindrance during anion uptake, as discussed earlier. During both charging cycles, the discharge process reveals a sharp deintercalation peak at 4.85 V and a broad peak within the voltage range of 4.33–3.90 V, signifying the reverse process of anion deintercalation from the graphite electrode and highlighting the intricacies of the intercalation/deintercalation mechanisms.

Ex situ structural investigations of FSA^--graphite intercalation compounds

To gain deeper insights into the processes of FSA^- intercalation/deintercalation in graphite-positive electrodes using the molten salt electrolyte, *ex situ* XRD measurements were conducted on Li||GrAl half-

View Article Online
DOI: 10.1039/D6TA00159A

cells at different SOC. Throughout the charging phase, FSA^- from the electrolyte, actively intercalates into the graphite-positive electrode. The intercalation and deintercalation of FSA^- result in the formation of $C_x^+(FSA^-)$ graphite intercalation compounds (GICs).

In the *ex situ* diffractograms (**Figure 2e**), the (002) diffraction peak of the pristine graphite sample is observed at 26.5°, corresponding to a d-spacing value of 3.36 Å. At 4.65 V vs. Li/Li^+, two new 2θ reflections emerge at 24.1° and 30.05°. Following the staging mechanism proposed for anion intercalation, well-studied in the intercalation of FSA^- anion via in situ XRD from ionic liquid electrolytes or HCEs, the dominant staging phase is determined by calculating the ratio of the $d_{(n+2)}/d_{(n+1)}$ peak positions[77–79]. The ratio for the charged graphite electrode corresponds to a value of 1.26, indicating a dominant stage-3 GIC. Mixed-stage structures (Stage 2 and Stage 3) and (Stage 2 and Stage 1) are observed at 4.75 V and 4.95 V, respectively, indicating an ongoing stage transition. Upon further charging to 5.1 V and 5.2 V, the 2θ reflections further shift to 22.4° and 34°, demonstrating the formation of a stage-1 GIC. The calculated values for the periodic repeat distance (I_c), gallery height (d_i), and gallery expansion (Δd) are presented in **Table S1** in SI. The repeat distance (I_c) values suggest a d_i value for the intercalation of FSA^- anions between graphene layers, approximately 7.9–8.2 Å. This significant increase in the interlayer distance of graphite from 3.36 Å to 7.9 Å, corresponding to an expansion of 135.5%, elucidates the challenges encountered during the initial anion uptake. However, the GrAl electrode using LE continues to exhibit a Stage 2 structure even after charging to 5.2V (**Figure S3d** in SI). Upon full discharge in MSE, a peak with slightly lower intensity appears at 26.4°, corresponding to a d-spacing value of 3.37 Å. The decreasing peak intensity and the shift to a lower 2θ, compared to the corresponding peak of pristine graphite, suggest a degree of irreversible expansion of the graphite galleries, or graphite exfoliation, upon anion (de)-insertion. This is consistent with previous reports of anion intercalation, where anions such as FSA^- and $TFSA^-$ have been shown to intercalate reversibly into graphite, while exfoliating it, and achieve lifetimes of 100 cycles or greater.[80–82]

To explore the parasitic reactions occurring on the graphite surface – especially at the high voltages needed for anion intercalation – potentiostatic tests were conducted employing Li||GrAl half cells with both MSE and LE (**Figure 2f**). The cells were charged from 3 to 6 V and were maintained at each voltage for 3

View Article Online
DOI: 10.1039/D6TA00159A

hours, with voltage steps of 0.2V. Notably, the cell utilizing MSE exhibits a leakage current of around 3 μA/cm^2 up to 6.0 V, indicating minimal electrolyte decomposition and positioning this MSE as a promising electrolyte option for high-voltage batteries. In contrast, the cell employing the LE displays a jump in current at 4.4V, attributed to the high degree of oxidative decomposition of carbonate solvents. Similarly, the potentiostatic tests were conducted employing Li||Al setups with both MSE and LE (**Figure S3e** in SI). The leakage current of the cell using LE is higher than the MSE cell in the voltage range investigated, and it shows a significant increase in current after 5.4V, while the current of the MSE cell is minimal and stable up to 6V.

Cycling of alkali cation intercalation in Li||GrCu half-cells

Li||GrCu half cells for alkali cation intercalation were cycled at various current densities to investigate the rate capabilities of the ternary molten salt electrolyte (**Figure 3a** and **Figure S4a-c** in SI) and liquid electrolyte (**Figure S4d-e** in SI). Each half cell was cycled 5 times at each current density from 50 mA g^{-1} to 400 mA g^{-1} (~0.29 to 2.37 mA cm^{-2}), with the current density increasing in steps of 50 mA g^{-1} after formation cycles. The half-cells were then cycled at 100 mA g^{-1} for 5 cycles to examine the recovery of the half-cell capacity. At a current density of 50 mA g^{-1}, a discharge capacity of ~370 mAh g^{-1} could be achieved, slightly lower than the theoretical capacity of lithium intercalated in graphite (372 mAh g^{-1}) but double compared to that of the cells using LE. Remarkably, at a current density four times higher (200 mA g^{-1}), half-cells could still deliver a discharge capacity of ~190 mAh g^{-1}, approximately half of the theoretical capacity of graphite. Even after 5 cycles at 400 mA g^{-1}, half-cells were able to recover and deliver a specific capacity of 260 mAh g^{-1} at 100 mA g^{-1}, which is similar to the specific capacity delivered at the previous set of cycles at 100 mA g^{-1} and ~70% of the theoretical capacity of lithium intercalated in graphite. Meanwhile, the cell using LE exhibits a noticeable decline in discharge capacity to 70 mAh g^{-1} at a current of 100 mA g^{-1}, later decreasing to below 20 mAh g^{-1} in the current of 200-400 mA g^{-1} (**Figure S4d** in SI). Interestingly, the CE (**Figure S4a** in SI) of the lithiation/delithiation into graphite using MSE at different current densities exhibits a promising value of approximately 99.7% (measured from the 2nd cycle at each current).

View Article Online
DOI: 10.1039/D6TA00159A

The cyclability of these Li||GrCu cation intercalation half-cells using the ternary molten salt electrolyte was investigated during long-term cycling over 100 cycles at a current density of 100 mA g^{-1} (**Figure 3b** and **Figure S4c** in SI). These half-cells are able to initially deliver a specific capacity of 300 mAh g^{-1} and slightly reduce to 270 mAh g^{-1} with an average CE of 99.6% over 100 cycles, indicating good lithium (de)intercalation reversibility and passivation of the graphite electrode. This ternary molten salt electrolyte can therefore support long-term, high-rate lithium insertion into graphite for high-performing DIBs. Meanwhile, Li||GrCu half-cells using the LE at a current density of 100 mA g^{-1} deliver a discharge capacity of 100 mAh $g^{-1,}$ which decreases by half after 20 cycles and stabilizes at 25 mAh g^{-1} after 100 cycles (**Figure S4e** in SI). Additionally, the CE of the cells using LE shows large fluctuations, indicating poor lithium (de)intercalation reversibility and passivation of graphite electrodes using this LE.

Cycling of FSA^- intercalation in Li||GrAl half cells

The rate performance of Li||GrAl half-cells was assessed at 80°C within the voltage range of 3.0–5.2 V with different current rates (**Figure 3c**). The CE and voltage profiles can be found in **Figure S4f** and **S4g** in SI, respectively. During the initial charge-discharge cycles with a current of 20 mA g^{-1}, the cell exhibits a substantial discharge capacity of 94 mAh g^{-1}. Upon transitioning the current to 50 mA g^{-1}, a noticeable decrease in capacity is observed, resulting in a discharge capacity of 52 mAh g^{-1} for the 10^{th} cycle. Notably, the CE remains stable at >98% across different high current rates, suggesting the formation of stable CEI layers on the graphite cathodes. Higher current rates prove advantageous in minimizing the time at elevated potentials (>5.0 V vs. Li/Li^+) and subsequent side reactions arising from electrolyte decomposition, as evidenced by the stable CE. **Figure 3d** illustrates the long-term FSA^- (de)intercalation cycling performance of Li||GrAl half cells using MSE at 50 mA g^{-1} and 80 °C. Remarkably, the discharged capacity stabilizes at 50 mAh g^{-1} after enduring 100 cycles, signifying a capacity retention rate of 82% relative to the capacity in the first cycle at 50 mA g^{-1}. The congruence of charge-discharge profiles, as depicted in **Figure S4h** in SI, shows a small decrease in voltage hysteresis between cycles, suggesting the consistent performance of GrAl electrodes cycled with MSE. The long-term cycling performance of Li||GrAl half cells using LE at a current rate of 50 mA g^{-1} at 20 °C was also determined (**Figure 3d**; this electrolyte enables a lower but stable

View Article Online
DOI: 10.1039/D6TA00159A

discharge capacity of 35 mAh g^{-1} with a CE close to that of the MSE cells. The effect of operation temperature on electrode kinetics was also examined. The electrochemical performance of Li||GrCu and Li||GrAl half-cells was investigated at 100 °C and compared with that at 80 °C (**Figure S4i**). As anticipated, the Li||GrCu cells delivered higher capacities at current densities above 50 mA g^{-1} when operated at 100 °C.

The self-discharge behavior of Li||GrAl cells in two electrolytes was studied to investigate the presence of parasitic reactions that deplete cell energy at high potentials. The experimental procedure involves charging the cells to 5.2 V, allowing them to rest for varied durations, and subsequently discharging them to 3 V to ascertain the remaining discharge capacity. The results of the self-discharge rate (denoted as *r*, representing the rate of capacity loss over time) are shown in **Figure S5a** in the SI. A stark contrast in the self-discharge behavior between the two electrolytes was observed after a 3-hour rest period: cells with LE exhibited a self-discharge rate of 32%/h, significantly higher than the 7%/h rate observed for cells utilizing MSE. This disparity is further evidenced by the corresponding decrease in battery voltage during the rest period (**Figure S5b** in SI), indicating a more pronounced self-discharge in LE cells, likely due to electrolyte solvent-driven side reactions under elevated voltages. Notably, an increase in resting time led to a decrease in the self-discharge rate, suggesting a diminution in electrolyte decomposition as a contributory factor to self-discharge at lower battery voltages.

View Article Online
DOI: 10.1039/D6TA00159A

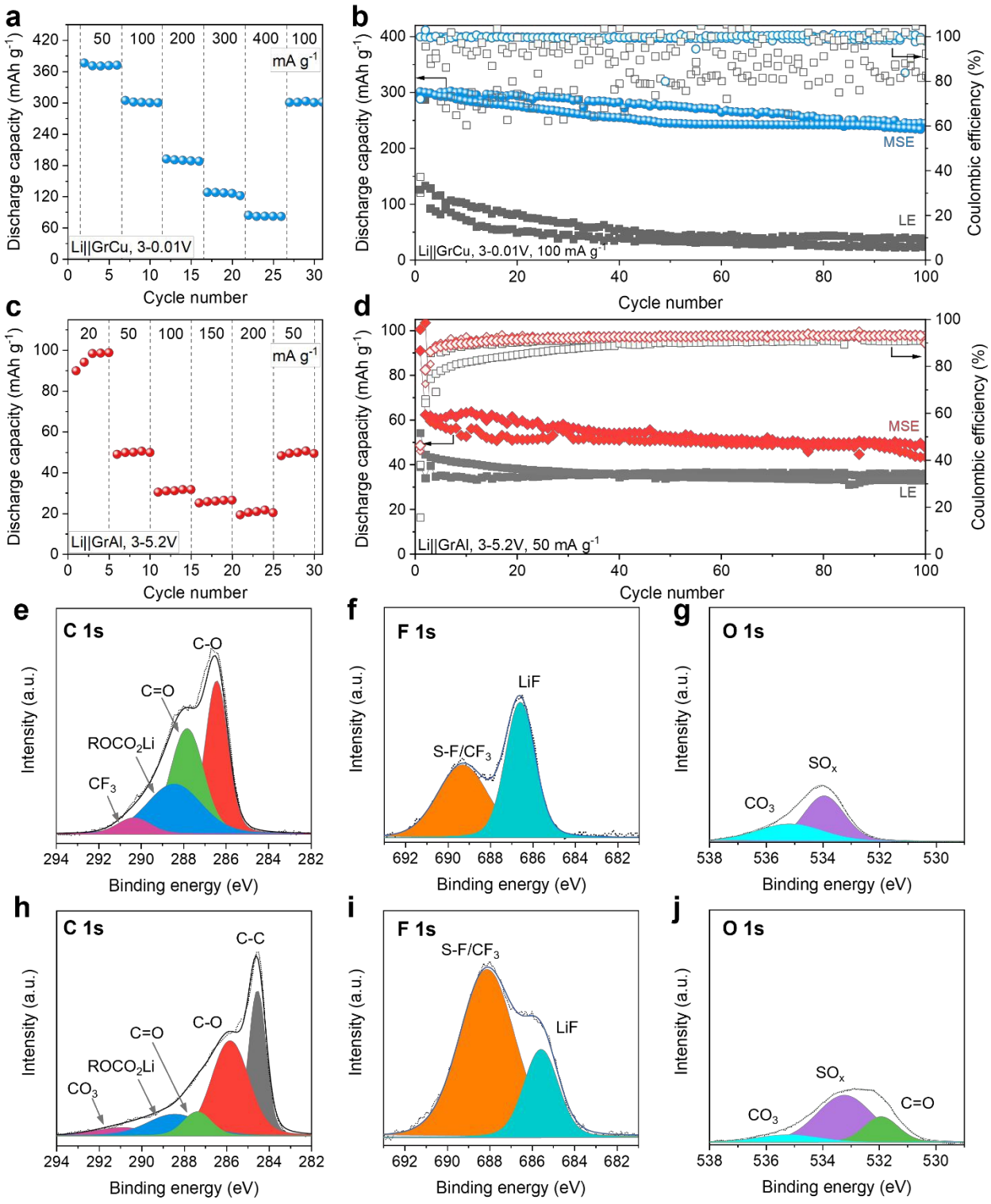

Figure 3. Half-cell cycling. (a) Discharge capacities of the Li||GrCu cells using MSE at different current densities in the voltage range of 0.01-3V (vs. Li/Li^+). (b) Long-term cycling of Li||GrCu cells using MSE and LE at 100 mA g^{-1}in the voltage range of 0.01-3V (vs. Li/Li^+). (c) Discharge capacities of the Li||GrAl

View Article Online
DOI: 10.1039/D6TA00159A

cells using MSE at different current densities in the voltage range of 3-5.2V (vs. Li/Li^+). (d) Long-term cycling of Li||GrAl cells MSE and LE at 50 mA g^{-1} in the voltage range of 3-5.2V (vs. Li/Li^+). (e-g) High-resolution X-ray photoelectron spectroscopy (XPS) of (e) C 1s, (f) F 1s, and (g) O 1s of the GrCu electrodes from the Li||GrCu cells using MSE at 100 mA g^{-1} in the voltage range of 0.01-3V (vs. Li/Li^+) after 100 cycles lithiation/delithiation. (h-j) High-resolution XPS of (h) C 1s, (i) F 1s, and (j) O 1s of the GrAl electrodes from the Li||GrAl cells MSE at 100 mA g^{-1} in the voltage range of 3-5.2V (vs. Li/Li^+) after 100 cycles of lithiation/delithiation.

To understand the mechanism behind the improved Li^+/FSA^- storage performances of the ternary molten salt system, the evolution of graphite electrodes after cycling was characterized using electrochemical impedance spectroscopy (EIS). EIS of the cycled GrCu and GrAl electrodes was used to delve into the charge transfer kinetics of the intercalation reactions. The Nyquist plots revealed the presence of a semicircle feature within the high-frequency domain, serving as a critical indicator of charge transfer processes. Notably, the semicircle radius, which correlates with charge-transfer resistance, was observed to expand after long-term cycling. As depicted in **Figures S5c-f** in SI, for Li||GrCu cells using MSE at 80 °C, R_{ct} increases slightly from 5.43 Ω (30^{th} cycle) to 6.35 Ω (100^{th} cycle), indicating stable interfacial kinetics. In contrast, LE measured at 25 °C shows a larger resistance and a more pronounced increase upon cycling (16.72 Ω to 19.31 Ω), suggesting greater interfacial degradation. These results indicate improved interphase stability in the MSE system under its operating conditions.

Furthermore, the elemental compositions of the cycled graphite electrodes were analyzed. X-ray photoelectron spectroscopy (XPS) of GrCu electrodes after the formation cycles and the 100^{th} cycle from the Li||GrCu half-cells using MSE and LE was performed. The high-resolution XPS of the pristine GrCu electrode (**Figure S6a-c** in SI) shows a minor amount of oxygen-containing groups (COOH, C-O-C, and OH). For GrCu electrodes using LE after formation cycles, the high-resolution C 1s, F 1s, and O 1s spectra show enhanced intensity of the peaks for Li-based organic species Li-O, C-O, C=O, and SO_x, compared to the pristine samples, indicating electrolyte solvent decomposition (**Figure S6d-f** in SI). However, the intensities of these peaks decreased, and the Li-F peak even disappeared after 100 cycles (**Figure S6g-i** in

View Article Online
DOI: 10.1039/D6TA00159A

SI), suggesting poor passivation of the electrode and continuous electrolyte degradation during long-term cycling. In contrast, for electrodes with MSE (**Figure S6j-l** in SI), the lower intensities for organic compounds and a higher intensity of the Li-F peak compared to those of the LE can be observed. After 100 cycles (**Figure 3e-g**), the peak intensities remain stable compared to those after formation cycling, indicating a significant suppression in the decomposition of electrolytes due to the stable SEI layer formation because of a high proportion of inorganic compounds (LiF, Li_2O). These inorganic constituents may contribute to the robustness of the SEI layer, thereby preserving the integrity of the electrolyte and enhancing overall electrochemical performance.

XPS was also performed to elucidate the chemical composition of the CEI. The high-resolution spectra (C 1s, O 1s, and F 1s) of the pristine graphite cathodes (**Figure S7a-c** in SI), and GrAl electrodes cycled using LE (**Figure S7d-f** in SI) and MSE (**Figure 3h-j**) are shown after 100 cycles. The spectra revealed, apart from the predominant peak associated with sp^2-hybridized carbon, the presence of various carbonaceous functional groups, including C-O, C=O, $ROCO_2Li$, Li_2CO_3, and CF_3. These are indicative of carbonate solvent decomposition prevalent in GrAl electrodes interfaced with LE. [83]**Figure 3i** shows that the LiF content in the CEI film cycled in MSE is significantly higher than LE, contributing to a stable CEI layer and enabling superior rate performance of MSE over LE.

Dual-graphite battery performance

To demonstrate the possibility of DGB with MSE for practical applications, a graphite||graphite battery was constructed as a proof of concept. DIBs are particularly sensitive to irreversible degradation reactions, as such reactions on either electrode can lead to the irreversible intercalation of ions at the counter electrode, causing capacity loss as the inventory of intercalation sites decreases. Therefore, pre-cycling of the anode (GrCu) to pre-form an SEI and/or establish an excess lithium inventory is undertaken to prolong the lifetime of DGBs[73]. To compare and better understand the different pre-cycling protocols reported in the literature, we used three different methodologies to pre-treat the GrCu anode in a Li||GrCu cell (**Figure S8**): 1) cycling

View Article Online
DOI: 10.1039/D6TA00159A

three times to pre-form an SEI without an excess Li inventory (denoted DGrCu in a half cell, DGr||Gr in a cell paired with a GrAl cathode), 2) cycling three times before partial lithiation of the anode to 0.09 V (denoted PGrCu in a half cell, PGr||Gr in a cell). These GrCu electrodes were then extracted from the half-cells and used to construct a cell by pairing them with a GrAl electrode. Un-treated GrCu electrodes were also cycled as controls. The cycling performance of each of these three types of DGB coin cells is illustrated in **Figure 4a**.

To understand the intercalation of cation/anion into graphite electrodes, the cells with precycled Gr||Gr were first charged to 5.2V, electrodes were collected, and then XRD and morphology characterizations were performed. **Figure 4b** shows that the precycled GrCu electrodes were charged to a higher degree of lithiation. Although pristine GrCu and DGrCu electrodes have no lithiated graphite compounds, the XRD pattern of the DGrCu electrode exhibits a small fraction of LiC_6, while that of the charged pristine GrCu electrode mainly exhibits LiC_{12} and $LiC_{18,}$ indicating that some Li^+ was lost to form the SEI layer on the graphite surface. Similarly, the PGrCu electrode shows the LiC_6 feature after charging to 5.2V. Interestingly, the XRD patterns of the GrAl cathodes from the precycled GrCu||GrAl cells at 5.2V show Stage 1 of anion intercalation in graphite, which is similar to anion intercalation behavior in the Li||Gr@Al cells, indicating full anion intercalation into graphite (**Figure 4c**). However, the pristine Gr||Gr cell shows a mixture of Stages 1-3.

Figure S8 in SI shows photos of the precycled GrCu electrodes after being charged, in which the pristine GrCu and DGrCu electrodes are mainly black in color, indicating a low degree of Li^+ intercalation into the graphite structure. Strikingly, the charged PGrCu electrode turns to a golden color attributed to the formation of a high degree of lithiation (e.g., LiC_6), which is similar to the full lithiation graphite color (**Figure S2** in SI). The morphologies (scanning electron microscopy, SEM) (**Figure 4d-f**) and elemental mapping from electron dispersive X-ray spectroscopy (EDS) (**Figure 4g-i**) of the charged anodes were also studied. The anodes of Gr||Gr and DGr||Gr cells exhibit a rough surface but a low expansion of graphite structure because of the low degree of lithiation, while the charged PGrCu electrode shows a large expansion of the graphite electrode.

View Article Online
DOI: 10.1039/D6TA00159A

The precycled Gr||Gr cells show similar redox characteristics to Li||GrAl cells (**Figure S9a** in SI). The precycled cells exhibit initial charge capacities of approximately 200 mAh g^{-1} and discharge capacities of around 95 mAh g^{-1} at a current density of 20 mA g^{-1} (with respect to the mass of the GrAl cathode) as seen in **Figure 4j**. The initial CEs of the Gr||Gr, DGr||Gr, and PGr||Gr cells are ~14%, ~48%, and ~48%, respectively. This performance is notably proximate to the theoretical specific capacity of FSA^--intercalated graphite, estimated at ~108 mAh g^{-1}[148]. However, the CE observed is relatively low, around 50%, attributable primarily to electrolyte decomposition and the subsequent formation of CEI/SEI films on the graphite surface[84]. Despite this, **Figure 4j** shows that the precycled Gr||Gr cells demonstrate superior rate capabilities, with discharge capacities exceeding 60 mAh g^{-1} (PGr||Gr), and over 50 mAh g^{-1} (DGr||Gr) at 50 mA g^{-1}. Remarkably, these cells maintain a discharge capacity of 30 mAh g^{-1} at elevated current densities of 200 mA g^{-1}, underscoring enhanced cell reaction kinetics. **Figures S9b-c** show the expected increased cell polarization with rising current densities for each cell architecture. Additionally, a marginal decline in the discharge capacity of the DGr||Gr cells after 75 cycles may be due to a depletion of active sites for ion intercalation as the interphases re-form with each successive cycle through irreversible reactions.[85] Over 100 cycles at 50 mA g^{-1} (**Figure 4k and Figure S9d-f)**, the precycled Gr||Gr cells sustain a reversible discharge capacity of ~50 mAh g^{-1} at an upper cutoff potential of 5.2 V. Cycling profiles of the various cell architectures up to 200 cycles are provided in Figure S10. After 100 cycles, the capacity of the DGr||Gr cell continues to decay gradually to ~30 mAh g^{-1}, whereas the capacity of the PGr||Gr cell remains at ~50 mAh g^{-1} up to 170 cycles, after which there is a sharp decline, similar to that exhibited by the DGr||Gr cells at 75 cycles, in capacity to ~30 mAh g^{-1}. Whereas the depletion of active sites for ion intercalation occurs earlier for DGr||Gr, we hypothesize that due to the excess Li in the PGr||Gr cells, any irreversibly stored anions or cations can be, in a sense, "recovered" by the de-intercalation of Li^+ from the reservoir.[85] This mitigates capacity fading, enabling higher discharge capacities for longer. Due to the nearly identical pre-formation process used to make the DGr||Gr and PGr||Gr anodes, we attribute this difference in performance solely to Li^+ doping as opposed to any difference in the interphasial properties.

View Article Online
DOI: 10.1039/D6TA00159A

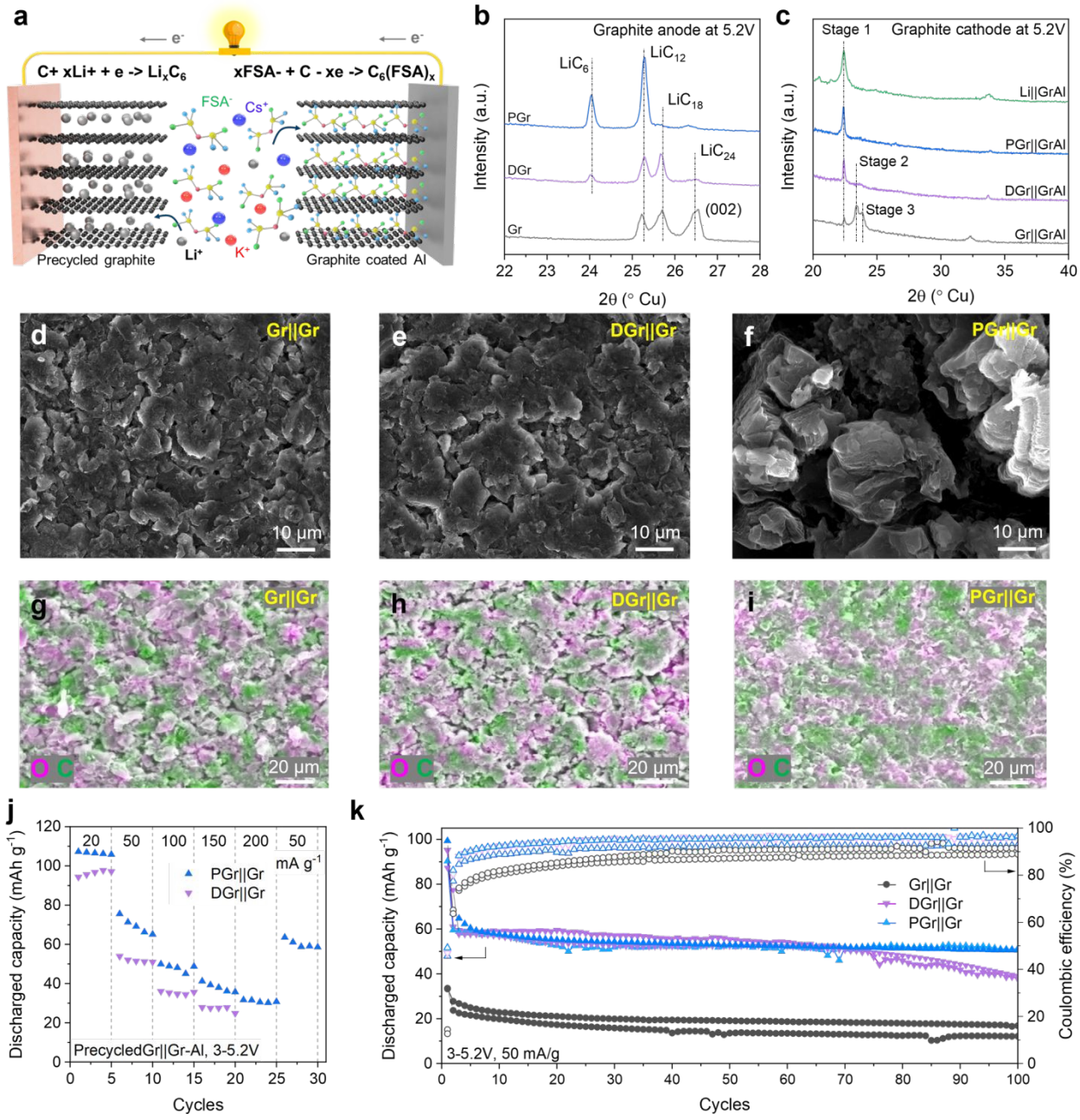

Figure 4. **Dual-graphite cell cycling**. (a) Schematic illustration of DGB with a precycled GrCu electrode coupled with a pristine GrAl electrode. (b, c) Ex-situ XRD of (b) the precycled GrCu electrodes and (c) GrAl electrodes of the cells DGB after being charged to 5.2V using MSE at 20 mA g^{-1}. (d-f) SEM images and (g-i) EDS images of oxygen (purple) and carbon (green) of the precycled GrCu electrodes from different types of DGBs after being charged to 5.2V using MSE at 20 mA g^{-1}. (j) Discharge capacities of the different types of DGB cells using MSE at different current densities in the voltage range of 3-5.2V (vs. Li/Li^+). (k) Long-

View Article Online
DOI: 10.1039/D6TA00159A

term cycling of the different types of DGB cells using MSE at 50 mA g^{-1} in the voltage range of 3-5.2V (vs. Li/Li^+). Multiple coin cells are shown.

Conclusions

We show a new battery chemistry with no transition metals and no solvent, which uses graphite as both an anode and a cathode that can be supported by a low-melting-point inorganic molten salt electrolyte. Using a suite of characterization tools, we show that in a $Li_{0.3}K_{0.35}Cs_{0.35}FSA$ molten salt, reversible (de)intercalation of both Li^+ cation and FSA^- anion into graphite occurs, which leads to high cell voltages (~5.2 V) and efficient charge storage. Additionally, the solventless molten salt electrolyte demonstrates good oxidative stability and good compatibility with graphite electrodes by forming a stable CEI/SEI layer on the graphite surface and suppresses self-discharge. As a result, the dual-graphite batteries enable stable cycling with discharge capacities greater than 50 mAh g^{-1} at 50 mA g^{-1}. This solvent-free, low-melting molten salt is a step towards achieving intrinsically energy-dense, transition metal-free dual-ion batteries.

View Article Online
DOI: 10.1039/D6TA00159A

Experimental

Electrolyte Preparation

The lithium bis(fluorosulfonyl)amide (LiFSA) salt (>99%) was sourced from Arkema (France). Potassium bis(fluorosulfonyl)amide (KFSA), purity of >99%, was procured from FUJIFILM Wako Pure Chemical Corporation (Japan) and cesium bis(fluorosulfonyl)amide (CsFSA) salt with a purity >98% was acquired from Provisco CS S.R.O. (Czech Republic). All salts underwent a drying process at 90 °C for 3 days under active vacuum within an integrated heating antechamber. Subsequently, they were securely stored in an Argon-filled glovebox (VigorTech) where both oxygen (O_2) and water (H_2O) content were maintained below 1 ppm. Karl–Fischer titration was performed to verify the water content in each salt remained below 20 ppm.

The preparation of the molten salt LiKCsFSA involved a procedure wherein the salts were mechanically combined with a mortar and pestle in the Ar-filled glovebox in a molar ratio of 30:35:35, respectively. The salt in a glass vial was melted on a hot plate at 120°C for 5 min and stored in the Ar-filled glovebox for prolonged usage.

All components of the coin cell (CR2032), including the negative case, Al-coated positive case, spring, and stainless-steel spacer (SS), were procured from Xiamen TOB New Energy Technology (China). The lithium foil, with a thickness of 500 µm and a purity of 99.9%, was purchased from China Energy Lithium Co., Ltd, and served as the reference/counter electrode. The lithium foil was brushed prior to use to eliminate oxide layers and was subsequently cut into disks measuring 12 mm in diameter. Celgard 3501 separators (25 µm thick, Celgard Co.) were obtained and cut into 18 mm disks, then subjected to vacuum drying at 60°C for 12 hours before use. Working electrodes (WE) including graphite-coated aluminum (GrAl), and graphite-coated copper (GrCu) were supplied by the Cell Analysis, Modeling, and Prototyping (CAMP) facility at Argonne National Laboratory.

The GrCu electrode exhibits a total mass loading of approximately 6.35 mg cm^{-2} and a coating thickness of 46 µm. The composition comprises 91.83 wt% graphite (Hitachi MagE3), 2 wt% Timcal C45 carbon, 6

View Article Online
DOI: 10.1039/D6TA00159A

wt% Kureha 9300 PVDF binder, and 0.17 wt% oxalic acid. The GrAl electrode has a total mass loading of around 6.39 mg cm^{-2} and a coating thickness of 42 μm. The composition includes 91.83 wt% Superior Graphite SLC1506T, 2 wt% Timcal C45 carbon, 6 wt% Kureha 9300 PVDF binder, and 0.17 wt% oxalic acid. Both electrodes were cut into 12 mm diameter disks and were dried under active vacuum overnight at 120 °C before use.

Coin Cell Assembly

Coin cells were assembled as follows: First, a spring and two pieces of stainless steel (SS) were added inside the negative casing, which was then placed on a hot plate set at 120 °C. Subsequently, the anode (lithium (Li), graphite-coated copper (GrCu), or precycled GrCu electrodes) was placed atop the SS spacer. Approximately 20 mg of molten salt electrolyte was poured and allowed to melt on the surface of the anode. Then, the separator was carefully situated on the molten electrolyte, ensuring that it was fully wet by applying light pressure. Next, an additional 30 mg of electrolyte was poured onto the separator surface, and the cathode was then placed face down on top of the separator. Finally, the Al disk and the Al-coated positive case were sequentially placed, and the cell was assembled under a pressure of 900 MPa using the TOB-DF-160 assembly tool from Xiamen TOB New Energy Technology Co., Ltd.

Characterization

For ex situ characterization, the graphite electrodes were intercalated at a current density of 20 mA g^{-1} to various cutoff potentials (vs. Li/Li^+). A Biologic MPG-2 potentiostat operated at 80°C was used for intercalation. The coin cells, after undergoing the charge/discharge cycles, were carefully transferred to the surface of a hot plate preheated to 120 °C within an Ar-filled environment for 5 minutes. Subsequently, the cells were disassembled using an electric crimping machine (TOB-DF-160, Xiamen TOB New Energy Technology Co., Ltd.), and the electrodes were carefully collected. For cation-intercalated graphite electrodes, these electrodes were immersed in the 1,2-Dimethoxyethane solvent (DME, Sigma Aldrich) for 30 seconds, repeated five times, to eliminate residual electrolyte. The washed electrodes were then placed in glass vials and subjected to vacuum drying within the glove box for 5 minutes. In contrast, anion-

View Article Online
DOI: 10.1039/D6TA00159A

intercalated graphite electrodes were characterized without undergoing the washing process due to observed self-discharge.

Ex-situ X-ray diffraction (XRD)

Ex-situ X-ray diffraction (XRD) analysis of the intercalated graphite electrodes was performed using a Rigaku SmartLab X-ray diffractometer. The instrument was equipped with a HyPix3000 detector and operated with Cu Kα (1.54186 Å) radiation at 40 kV and 40 mA. Scans were conducted with a 2θ step of 0.05 over the range of 10-80° at a scan rate of 10°/min. For the XRD analysis, the graphite sample was carefully positioned on top of a Kapton board and covered with polyimide tape (0.0025 in thickness) before being transferred out of the glovebox for testing.

Raman spectroscopy

Ex-situ Raman spectroscopy of the intercalated graphite electrodes at various cut-off voltages was conducted using a LabRAM HR Raman spectrometer with laser excitation at 633 nm. To ensure the integrity of the measurements, the graphite sample was sealed in glass chambers within an argon-filled glovebox. The glass chamber assembly utilized glass slides obtained from Chemglass Life Science and silicone isolators purchased from Grace Bio-Labs.

X-ray photoelectron spectroscopy (XPS)

X-ray Photoelectron Spectroscopy (XPS) was employed to analyze the chemical compositions of the intercalated graphite electrodes. The XPS characterization was carried out utilizing the PHI 5000 VersaProbe II System from Physical Electronics, equipped with an Al Kα radiation beam (hν = 1486.6 eV) with a diameter of 100 μm and a power of 25 W. The samples were prepared and mounted on the XPS holder using carbon tape. The obtained XPS spectra were further analyzed, and peaks were fitted using CasaXPS software for detailed interpretation and identification of chemical components.

Solid state magic angle spinning nuclear magnetic resonance spectroscopy (ssNMR)

^{7}Li ssNMR experiments were conducted utilizing a Bruker Avance III wide bore 400 MHz solid-state NMR spectrometer operating at 9.5 Tesla. To prepare the samples for NMR analysis, intercalated

View Article Online
DOI: 10.1039/D6TA00159A

graphite electrodes were carefully scraped off the substrate using a metal blade. The scraped material was then mechanically combined with potassium bromide (KBr, Sigma Aldrich) in a mass ratio of 10:90 (w/w). The resulting powder was packed into 1.9 mm zirconia rotors. During the NMR experiments, the rotors were spun at a rate of 20 kHz, and spectra were acquired with a recycle delay time ranging from 30 to 50 seconds, depending on the specific characteristics of the sample under investigation.

Inductively Coupled Plasma Mass Spectrometry (ICP-MS)

The ICP-MS technique was used to confirm the chemical compositions of the cations intercalated into the graphite electrodes. Samples were scraped out from the current collector with the help of a clean plastic spatula. The final graphite sample was weighed and placed into a ceramic crucible (Coors™ high-alumina crucible, Sigma) and heated to 700°C for 10 h in a high-temperature muffle furnace (KSL-1100X). The remaining ashes were digested with 10 ml of a 3% (v/v) HNO_3 solution (TraceMetal Grade, Thermo Fisher Scientific) for about 30 min. The same HNO_3 solution was used as a matrix for further dilutions. All ICP-MS measurements were performed either in a Thermo iCAP Q ICP-MS or Thermo iCAP RQ ICP-MS.

Morphology

Field Emission Scanning Electron Microscopy (SEM) employing the Carl Zeiss Merlin instrument with an accelerating voltage of 10 kV was employed to examine the morphology of the intercalated graphite electrode surface. Elemental distribution on the surface of electrodes was mapped with an Oxford UltimMax100 EDX spectroscopy sensor.

Dual-Graphite Cell Cycling

The charge/discharge current density was calculated based on the exact mass of graphite active material on electrodes. A Biologic MPG-2 potentiostat was used to cycle coin cells at temperatures of 80°C in the heating chambers of Memmert IN 110. For the cation intercalation using Li||GrCu cells, the cells performed 3 formation cycles at 20 mA g^{-1} and later cycled at the specific current densities with a voltage range of 0.01-3V (vs. Li/Li^+). For the anion intercalation using Li||GrAl cells, the cells performed 3 formation cycles at 20 mA g^{-1}. They later cycled at the different specific current densities (calculated based on the active mass of the GrAl electrode) with a voltage range of 5.2-3V (vs. Li/Li^+). For the cycling of dual-graphite cells, the

View Article Online
DOI: 10.1039/D6TA00159A

anode GrCu electrodes were first performed 3 formation cycles and then charged to different stages using the Li||GrCu cells including (1) charging to 0.09 V for partially lithiated graphite (PGr), (2) charging to 0.01 V for fully lithiated graphite (LGr), (2) discharging to 3 V for fully delithiated graphite (DGr). The precycled graphite electrodes were collected and served as the anode electrodes coupled with the pristine GrAl electrodes to form the dual-graphite battery cells. The cells performed 3 formation cycles at 20 mA g^{-1} and later cycled at the current density of 100 mA g^{-1} (calculated based on the active mass of the GrAl electrode) with a voltage range of 5.2-3 V (vs. Li/Li^+).

Acknowledgments

This work was supported by the US Department of Energy (DOE) Office of Basic Energy Sciences (Award number DE-SC0023258). E.S.D. and H.S.S. are supported by the NSF NRT AIMEMS Fellowship. This work made use of the shared facilities (SEM, XPS) at the University of Chicago Materials Research Science and Engineering Center, supported by the National Science Foundation under award number DMR-2011854. Solid state NMR experiments were performed at the University of Illinois at Chicago NMR facility (NIH award 1S10RR025105-01). The authors thank Steve Trask and Andrew Jansen at Argonne's Cell Analysis, Modeling, and Prototyping (CAMP) facility for providing the graphite electrode, and Gangbin Yan for performing ICP-MS.

Author contributions

M.C.V. and C.V.A. designed the experiments. M.C.V. and H.S.S. conducted electrochemical measurements. P.M. and E.S.D. conducted MAS-NMR experiments. R.J.G. prepared samples for and helped perform ICP-MS. C.V.A. conceived and supervised the project. M.C.V., H.S.S., and C.V.A. wrote the manuscript. All authors discussed the results and reviewed the manuscript.

Declaration of Interests

The authors declare no competing interests.

View Article Online
DOI: 10.1039/D6TA00159A

References

1 M. Li, J. Lu, Z. Chen and K. Amine, *Advanced Materials*, 2018, **30**, 1800561.

2 F. Duffner, N. Kronemeyer, J. Tübke, J. Leker, M. Winter and R. Schmuch, *Nat. Energy*, 2021, **6**, 123–134.

3 Q. Zheng, Y. Yamada, R. Shang, S. Ko, Y. Y. Lee, K. Kim, E. Nakamura and A. Yamada, *Nat. Energy*, 2020, **5**, 291–298.

4 H. Sun, G. Zhu, Y. Zhu, M. C. Lin, H. Chen, Y. Y. Li, W. H. Hung, B. Zhou, X. Wang, Y. Bai, M. Gu, C. L. Huang, H. C. Tai, X. Xu, M. Angell, J. J. Shyue and H. Dai, *Advanced Materials*, DOI:10.1002/ADMA.202001741.

5 Z. Zhao and H. N. Alshareef, *Advanced Materials*, 2024, **36**, 2309223.

6 T. HK and N. Hossiney, *Mater. Today Proc.*, 2022, **61**, 327–331.

7 E. Fan, L. Li, Z. Wang, J. Lin, Y. Huang, Y. Yao, R. Chen and F. Wu, *Chem. Rev.*, 2020, **120**, 7020–7063.

8 Wenyuan Qiao, Ren Zhang, Yikai Wen, Xinyi Wang, Zheng Wang, Guoqiang Tang, Minghao Liu, Hyokyeong Kang, Zafar Said, Jang-Yeon Hwang and Changhui Liu, *J. Mater. Chem. A Mater.*, 2024, **12**, 11235–11265.

9 Z. Chen, Y. Deng, J. Kong, W. Fu, C. Liu, T. Jin, L. Jiao, Z. Chen, Y. Deng, J. Kong, W. Fu, T. Jin, L. Jiao and C. Liu, *Advanced Materials*, 2024, 2402008.

10 C. Che, F. Wu, Y. Li, Y. Li, S. Li, C. Wu and Y. Bai, *Advanced Materials*, 2024, 2402291.

11 M. H. Hossain, N. Abdullah, K. H. Tan, R. Saidur, M. A. Mohd Radzi and S. Shafie, *The Chemical Record*, 2024, **24**, e202300092.

12 H. Wang, S. A. Pourmousavi, W. L. Soong, X. Zhang and N. Ertugrul, *J. Energy Storage*, 2023, **58**, 106384.

View Article Online
DOI: 10.1039/D6TA00159A

13 M. Pan, M. Shao and Z. Jin, *SmartMat*, 2023, **4**, e1198.

14 G. Yang, Y. Zhu, Z. Hao, Y. Lu, Q. Zhao, K. Zhang and J. Chen, *Advanced Materials*, 2023, **35**, 2301898.

15 K. Hatakeyama-Sato and K. Oyaizu, *Chem. Rev.*, 2023, **123**, 11336–11391.

16 M. Shi, P. Das, Z. S. Wu, T. gen Liu and X. Zhang, *Advanced Materials*, 2023, **35**, 2302199.

17 X. Ou, D. Gong, C. Han, Z. Liu and Y. Tang, *Adv. Energy Mater.*, 2021, **11**, 2102498.

18 D. Yu, K. Li, G. Ma, F. Ru, X. Zhang, W. Luo, P. Hu, D. Chen and H. Wang, *ChemSusChem*, 2023, **16**, e202201595.

19 D. Zhang, W. Zhang, S. Zhang, X. Ji and L. Li, *J. Energy Storage*, 2023, **60**, 106678.

20 T. Placke, A. Heckmann, R. Schmuch, P. Meister, K. Beltrop and M. Winter, 2018, **2**, 2528–2550.

21 K. V. Kravchyk and M. V. Kovalenko, *Adv. Energy Mater.*, DOI:10.1002/AENM.201901749.

22 J. Chen, H. Lan, S. Wang, X. Liu, Q. Zhu, X. Zhang, M. Tang, S. Dong, J. Yang, M. Kurbanov, L. Guo and H. Wang, *J. Am. Chem. Soc.*, 2025, **147**, 2393–2402.

23 M. Sheng, F. Zhang, B. Ji, X. Tong, Y. Tang, M. H. Sheng, F. Zhang, B. F. Ji, X. F. Tong and Y. B. Tang, *Adv. Energy Mater.*, 2017, **7**, 1601963.

24 X. Zhang, Y. Tang, F. Zhang, C.-S. Lee, X. L. Zhang, Y. B. Tang, F. Zhang and C. Lee, *Adv. Energy Mater.*, 2016, **6**, 1502588.

25 X. Li, X. Ou and Y. Tang, *Adv. Energy Mater.*, 2020, **10**, 2002567.

26 L. Xiang, X. Ou, X. Wang, Z. Zhou, X. Li and Y. Tang, *Angew. Chem. Int. Ed.*, 2020, **59**, 17924–17930.

27 D. Yu, Q. Zhu, L. Cheng, S. Dong, X. Zhang, H. Wang and N. Yang, *ACS Energy Lett.*, 2021, **6**, 949–958.

28 M. Armand, F. Endres, D. R. MacFarlane, H. Ohno and B. Scrosati, *Nat. Mater.*, 2009, **8**, 621–629.

View Article Online
DOI: 10.1039/D6TA00159A

29 S. Rothermel, P. Meister, G. Schmuelling, O. Fromm, H. W. Meyer, S. Nowak, M. Winter and T. Placke, *Energy Environ. Sci.*, 2014, **7**, 3412–3423.

30 R. S. Kühnel, M. Lübke, M. Winter, S. Passerini and A. Balducci, *J. Power Sources*, 2012, **214**, 178–184.

31 B. Garcia and M. Armand, *J. Power Sources*, 2004, **132**, 206–208.

32 S. T. Myung, Y. Hitoshi and Y. K. Sun, *J. Mater. Chem.*, 2011, **21**, 9891–9911.

33 K. Kubota and H. Matsumoto, *Journal of Physical Chemistry C*, 2013, **117**, 18829–18836.

34 K. Kubota and H. Matsumoto, *J. Electrochem. Soc.*, 2014, **161**, A902–A907.

35 K. Kubota and H. Matsumoto, *ECS Trans.*, 2014, **62**, 231–234.

36 K. Kubota and H. Matsumoto, *ECS Trans.*, 2016, **73**, 95–100.

37 R. T. Carlin, H. C. De Long, J. Fuller and P. C. Trulove, *J. Electrochem. Soc.*, 1994, **141**, L73–L76.

38 V. Giordani, D. Tozier, H. Tan, C. M. Burke, B. M. Gallant, J. Uddin, J. R. Greer, B. D. McCloskey, G. V. Chase and D. Addison, *J. Am. Chem. Soc.*, 2016, **138**, 2656–2663.

39 Y. Song, S. Jiao, J. Tu, J. Wang, Y. Liu, H. Jiao, X. Mao, Z. Guo and D. J. Fray, *J. Mater. Chem. A Mater.*, 2017, **5**, 1282–1291.

40 K. Kubota, T. Nohira and R. Hagiwara, *Electrochim. Acta*, 2012, **66**, 320–324.

41 M. C. Vu, P. Mirmira, R. J. Gomes, P. Ma, E. S. Doyle, H. S. Srinivasan and C. V. Amanchukwu, *Matter*, 2023, **6**, 4357–4375.

42 C.-Y. Chen, K. Matsumoto, K. Kubota, R. Hagiwara, Q. Xu, C.-Y. Chen, K. Matsumoto, K. Kubota, R. Hagiwara and Q. Xu, *Adv. Funct. Mater.*, 2020, **30**, 2003557.

43 F. Xu, C. Liu, W. Feng, J. Nie, H. Li, X. Huang and Z. Zhou, *Electrochim. Acta*, 2014, **135**, 217–223.

View Article Online
DOI: 10.1039/D6TA00159A

44 Q. Xu, C. Schwandt, G. Z. Chen and D. J. Fray, *Journal of Electroanalytical Chemistry*, 2002, **530**, 16–22.

45 J. Zhao, X. Zou, Y. Zhu, Y. Xu, C. Wang, J. Zhao, Y. H. Xu, X. Zou, Y. J. Zhu and C. S. Wang, *Adv. Funct. Mater.*, 2016, **26**, 8103–8110.

46 A. Yadav, H. Kobayashi, T. Yamamoto and T. Nohira, *Electrochemistry*, 2024, **92**, 043008–043008.

47 M. C. Vu, P. Mirmira, R. J. Gomes, P. Ma, E. S. Doyle, H. S. Srinivasan and C. V. Amanchukwu, *Matter*, 2023, **6**, 4357–4375.

48 Y. Zhao, K. Xue and D. Y. W. Yu, *Adv. Funct. Mater.*, 2023, **33**, 2300305.

49 H. Onuma, K. Kubota, S. Muratsubaki, W. Ota, M. Shishkin, H. Sato, K. Yamashita, S. Yasuno and S. Komaba, *J. Mater. Chem. A Mater.*, 2021, **9**, 11187–11200.

50 G. Wang, M. Yu and X. Feng, *Chem. Soc. Rev.*, 2021, **50**, 2388–2443.

51 H. Fujimoto, T. Yamaki, K. Shimoda, S. Fujinami, T. Nakatani, G. Kano, M. Kawasaki, Z. Ogumi and T. Abe, *J. Electrochem. Soc.*, 2022, **169**, 070507.

52 N. Li and D. Su, *Carbon Energy*, 2019, **1**, 200–218.

53 J. Xu, Y. Dou, Z. Wei, J. Ma, Y. Deng, Y. Li, H. Liu and S. Dou, *Advanced Science*, 2017, **4**, 1700146.

54 J. Hui, A. Nijamudheen, D. Sarbapalli, C. Xia, Z. Qu, J. L. Mendoza-Cortes and J. Rodríguez-López, *Chem. Sci.*, 2021, **12**, 559–568.

55 Y. Liu, B. V. Merinov and W. A. Goddard, *Proc. Natl. Acad. Sci. U. S. A.*, 2016, **113**, 3735–3739.

56 S. E. Pruvost, C. Hérold, A. Hérold and P. Lagrange, *Carbon N. Y.*, 2003, **41**, 1281–1289.

57 Y. Liu, B. V. Merinov and W. A. Goddard, *Proc. Natl. Acad. Sci. U. S. A.*, 2016, **113**, 3735–3739.

58 S. L. Jose Mendoza-Cortes, N. Li, J. Hui, A. Nijamudheen, D. Sarbapalli, C. Xia, Z. Qu, J. L. Mendoza-Cortes and J. ın RodríguezRodríguez-L, DOI:10.1039/d0sc03226c.

View Article Online
DOI: 10.1039/D6TA00159A

59 P. Ma, P. Mirmira, P. J. Eng, S. B. Son, I. D. Bloom, A. S. Filatov and C. V. Amanchukwu, *Energy Environ. Sci.*, 2022, **15**, 4823–4835.

60 Z. Jian, W. Luo and X. Ji, *J. Am. Chem. Soc.*, 2015, **137**, 11566–11569.

61 V. B. Cajipe, P. A. Heiney and J. E. Fischer, *Phys. Rev. B*, 1989, **39**, 4374.

62 J. Zou, C. Sole, N. E. Drewett, M. Velický and L. J. Hardwick, *Journal of Physical Chemistry Letters*, 2016, **7**, 4291–4296.

63 S. Jovanovic, P. Jakes, S. Merz, R. A. Eichel and J. Granwehr, *Electrochemical Science Advances*, 2022, **2**, e2100068.

64 X. Jiang, X. Liu, Z. Zeng, L. Xiao, X. Ai, H. Yang, Y. Cao, X. Jiang, X. Liu, Z. Zeng, X. Ai, H. Yang, Y. Cao and L. Xiao, *Adv. Energy Mater.*, 2018, **8**, 1802176.

65 M. Nádherná, J. Reiter, J. Moškon and R. Dominko, *J. Power Sources*, 2011, **196**, 7700–7706.

66 T. Placke, O. Fromm, S. F. Lux, P. Bieker, S. Rothermel, H.-W. Meyer, S. Passerini and M. Winter, *J. Electrochem. Soc.*, 2012, **159**, A1755–A1765.

67 K. Beltrop, X. Qi, T. Hering, S. Röser, M. Winter and T. Placke, *J. Power Sources*, 2018, **373**, 193–202.

68 L. L. Jiang, C. Yan, Y. X. Yao, W. Cai, J. Q. Huang and Q. Zhang, *Angew. Chem. Int. Ed.*, 2021, **60**, 3402–3406.

69 J. Li, C. Han, X. Ou and Y. Tang, *Angew. Chem. Int. Ed.*, 2022, **61**, e202116668.

70 H. Tan, D. Zhai, F. Kang and B. Zhang, *Carbon N. Y.*, 2021, **178**, 363–370.

71 Y. Wang, Y. Zhang, S. Dong, W. Zhou, P. K. Lee, Z. Peng, C. Dang, P. H. L. Sit, J. Guo and D. Y. W. Yu, *Adv. Energy Mater.*, 2022, **12**, 2103360.

View Article Online
DOI: 10.1039/D6TA00159A

72 G. Wang, B. Kohn, U. Scheler, F. Wang, S. Oswald, M. Löffler, D. Tan, P. Zhang, J. Zhang, X. Feng, G. Wang, F. Wang, P. Zhang, J. Zhang, X. Feng, B. Kohn, U. Scheler, S. Oswald, M. Löffler and D. Tan, *Advanced Materials*, 2020, **32**, 1905681.

73 Y. Wang, Y. Zhang, S. Wang, S. Dong, C. Dang, W. Hu and D. Y. W. Yu, *Adv. Funct. Mater.*, 2021, **31**, 1804766.

74 L. Fan, Q. Liu, S. Chen, K. Lin, Z. Xu and B. Lu, *Small*, 2017, **13**, 1701011.

75 J. A. Read, A. V. Cresce, M. H. Ervin and K. Xu, *Energy Environ. Sci.*, 2014, **7**, 617–620.

76 H. Li, T. Kurihara, D. Yang, M. Watanabe and T. Ishihara, *Energy Storage Mater.*, 2021, **38**, 454–461.

77 B. Ozmen-Monkul and M. M. Lerner, *Carbon N. Y.*, 2010, **48**, 3205–3210.

78 G. Schmuelling, T. Placke, R. Kloepsch, O. Fromm, H. W. Meyer, S. Passerini and M. Winter, *J. Power Sources*, 2013, **239**, 563–571.

79 P. Meister, V. Siozios, J. Reiter, S. Klamor, S. Rothermel, O. Fromm, H. W. Meyer, M. Winter and T. Placke, *Electrochim. Acta*, 2014, **130**, 625–633.

80 S. Rothermel, P. Meister, G. Schmuelling, O. Fromm, H.-W. Meyer, S. Nowak, M. Winter and T. Placke, DOI:10.1039/c4ee01873g.

81 P. Meister, G. Schmuelling, M. Winter and T. Placke, *Electrochem. commun.*, 2016, **71**, 52–55.

82 K. Beltrop, J. C. Madrid Madrid, P. Meister, A. Heckmann, M. Winter, T. Akbay, T. Ishihara and T. Placke, *J. Power Sources*, 2020, **469**, 228397.

83 W. Luo, D. Yu, T. Ge, J. Yang, S. Dong, H. Chen, L. Qin, Y. Huang and D. Chen, *Appl. Energy*, 2024, **358**, 122652.

84 J. Collins, G. Gourdin, M. Foster and D. Qu, *Carbon N. Y.*, 2015, **92**, 193–244.

85 B. Heidrich, A. Heckmann, K. Beltrop, M. Winter and T. Placke, DOI:10.1016/j.ensm.2019.05.031.

View Article Online
DOI: 10.1039/D6TA00159A

View Article Online
DOI: 10.1039/D6TA00159A

Data Availability Statement

The data supporting this article have been included as part of the Supplementary Information